

Gate controlled large resistance switching driven by charge density wave in 1T-TaS₂/2H-MoS₂ heterojunction

Mehak Mahajan^{||}, Krishna Murali^{||}, Nikhil Kawatra, and Kausik Majumdar^{*}

Department of Electrical Communication Engineering, Indian Institute of Science, Bangalore 560012, India

^{||}These authors contributed equally, ^{*}*Corresponding author*, email: kausikm@iisc.ac.in

ABSTRACT: 1T-TaS₂ is a layered material that exhibits charge density wave (CDW) induced distinct electrical resistivity phases and has attracted a lot of attention for interesting device applications. However, such resistivity switching effects are often weak, and cannot be modulated by an external gate voltage – limiting their widespread usage. Using a back-gated 1T-TaS₂/2H-MoS₂ heterojunction, here we show that the usual resistivity switching in TaS₂ due to different phase transitions is accompanied with a surprisingly strong modulation in the Schottky barrier height (SBH) at the TaS₂/MoS₂ interface – providing an additional knob to control the degree of the phase-transition-driven resistivity switching by an external gate voltage. In particular, the commensurate (C) to triclinic (T) phase transition results in an increase in the SBH owing to a collapse of the Mott gap in TaS₂. The change in SBH allows us to estimate an electrical Mott gap opening of $\sim 71 \pm 7$ meV in the C phase of TaS₂. On the other hand, the nearly-commensurate (NC) to incommensurate (IC) phase transition results in a suppression in the SBH, and the heterojunction shows a gate-controlled resistivity switching up to 17.3, which is ~ 14.5 times higher than that of standalone TaS₂. The findings mark an important step forward showing a promising pathway to externally control as well as amplify the CDW induced resistivity switching. This will boost device applications that exploit these phase transitions, such as ultra-broadband photodetection, negative differential conductance, fast oscillator and threshold switching in neuromorphic circuits.

Keywords: Charge density wave (CDW), Transition metal dichalcogenide, 1T-TaS₂, MoS₂, Mott transition, Schottky barrier height.

Transition metal dichalcogenides are emerging out as pertinent materials for applications in high performance flexible electronics and optoelectronics^{1,2,3}. 1T-TaS₂ is a distinct layered material that exhibits multiple conductivity phases resulting from strong electron-phonon and electron-electron interactions. This material hosts a wide variety of charge density wave (CDW)^{4,5} states and the CDW amplitude is significant in 1T-polytype as compared to 2H-polytype of TaS₂^{6,7}. Depending on the temperature of the 1T-TaS₂ crystal, CDW exists in different phases subject to the alignment with the underlying lattice^{6,8,9,10}. As the temperature is reduced below 550 K, the metallic crystal undergoes a CDW phase transition, however the CDW remains incommensurate (IC) with the underlying crystal lattice. On further cooling, it undergoes IC to nearly-commensurate (NC) CDW phase transition at 340 K, and an NC to commensurate (C) phase transition at 180 K. The NC to C transition is accompanied with a Mott transition resulting in strong suppression of conductivity. On heating, the crystal undergoes a new phase transition, from C phase to the triclinic (T) phase appearing at 223 K^{11,12,13}, followed by a T to NC, and NC to IC phase transitions at 283 K and 353 K, respectively. The different CDW phase transitions can also be controlled by pressure^{8,14}, doping^{15,16}, thickness^{17,18} and photoexcitation^{9,19}.

Among these different phase transitions, the C-T transition is of great scientific interest due to a large resistivity switching of more than an order of magnitude^{7,8,18} owing to a Mott gap opening associated with the phase transition. While the Mott gap opening has been extracted by several reports using various optical techniques^{9,10,20,21,22,23,24,25}, an estimation of the electrical gap directly from transport measurement of a TaS₂ device is missing. On the contrary, the NC-IC transition can be electrically driven while operating at room temperature and thus has attracted a lot of attention in device applications, including wideband photodetector²⁶, fast oscillator²⁷ and neuromorphic circuits²⁸. However, there are two intrinsic bottlenecks with such resistivity

switching. First, the resistivity switching ratio during the NC-IC phase transition is quite weak (< 2)^{7,8,18}. Second, the phase transition driven resistivity switching of TaS₂ cannot be controlled by an external gate voltage. Hence, improving the switching ratio in the NC-IC phase transition and adding a possible gate controllability would be of great importance for the advancement of these applications.

In order to address these issues, in this work, we employ a 1T-TaS₂/2H-MoS₂ heterojunction (lattice mismatch of $\sim 6.33\%$ ^{29,30}) in a back gated field effect transistor (FET) structure. We show that the TaS₂/MoS₂ interface exhibits a low barrier, high performance van der Waals (vdW) electrical contact^{31,32,33,34,35,36}, which is promising for pathway towards “all-2D” flexible devices. We also demonstrate that both the C-T and NC-IC phase transitions not only result in a change in the resistivity in the TaS₂ film, but also bring about a change in the Schottky barrier height (SBH) at the TaS₂/MoS₂ interface. This allows us to control the phase transition driven carrier transport through the heterojunction device by the application of a gate voltage. The C-T phase transition results in an increase in the SBH, which allows us to electrically estimate the Mott gap opening in 1T-TaS₂ at the C phase. On the other hand, the NC-IC phase transition reduces the SBH at the TaS₂/MoS₂ interface, which, depending on the gate voltage applied, enhances the switching ratio by a factor as much as 14.5X compared with 1T-TaS₂ control.

Results and Discussions:

2H-MoS₂ is a layered transition metal di-chalcogenide (TMDC) semiconductor, which is appealing as a channel material in electronic device applications owing to its appreciable bandgap, moderate carrier mobility, and channel length scalability. The heterojunction device used in this work is schematically shown in Fig. 1a, where a back gated MoS₂ channel is formed with asymmetric contacts, namely Ni and TaS₂ contacts on two different sides. We note that Ni makes

good electrical contact with MoS₂^{37,38,39} (see **Supplemental Material S1**⁴⁰) owing to efficient interfacial charge transfer resulting from strong hybridization of partially filled Ni-3*d* and S-3*p* orbitals³⁹. By switching the polarity of the drain voltage, we study characteristics of the carrier injection through the TaS₂/MoS₂ contact interface while taking Ni/MoS₂ junction of the same device as the reference interface. To fabricate the heterojunction device, we first exfoliate few-layer 2H-MoS₂ flakes on 285 nm thick SiO₂ coated heavily-doped Si substrate. We next transfer thin layers of 1T-TaS₂ on top of the MoS₂ flake under a microscope using a micromanipulator. The contact electrodes are patterned by electron beam lithography, followed by electron-beam evaporation of Ni (10nm)/Au (50 nm), and subsequent lift-off. Fig. 1b shows the optical image of the device after completion of fabrication. The top panel of Fig. 1c depicts the corresponding thickness mapping image using Atomic Force Microscope (AFM). The bottom panel of Fig. 1c shows the thickness of the MoS₂ and the TaS₂ flakes are 6.4 nm and 43.6 nm, respectively, as measured along the green dashed arrow. The devices reported in this work are measured multiple times over a period of several weeks and no noticeable degradation of the device characteristics is observed due to surface oxidation and other ambience induced effects.

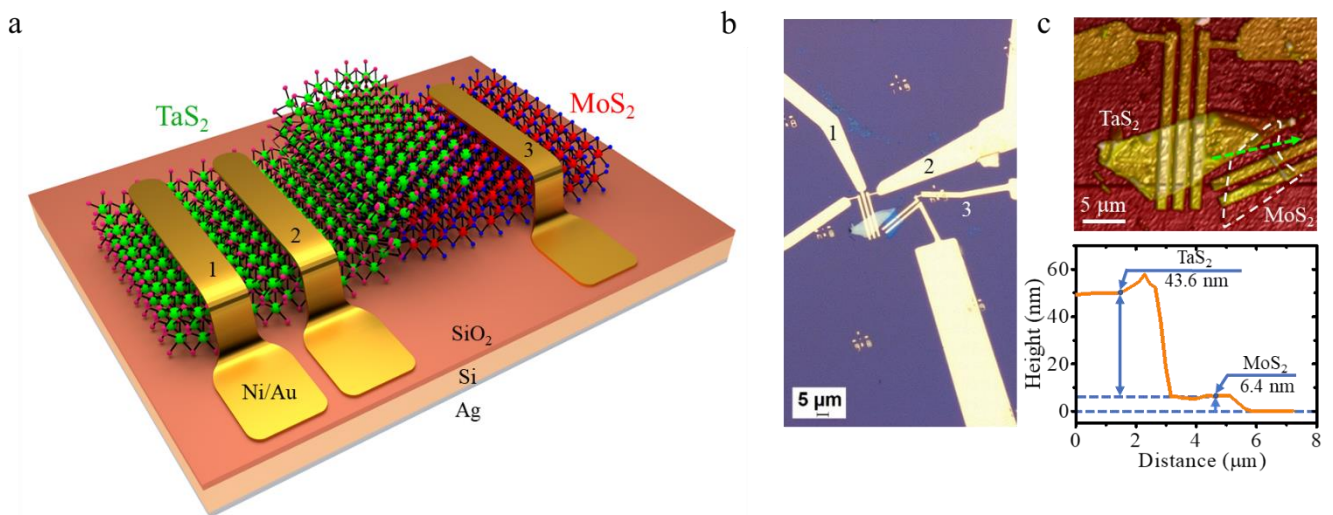


Figure 1. 1T-TaS₂/2H-MoS₂ heterojunction. (a) Schematic of the device with terminals 1 and 2 probing the TaS₂ control device (TS12) and terminals 2 and 3 probing the heterojunction device (H23). (b) Optical image of the fabricated device. Scale bar: 5 μm . (c) Top panel: AFM thickness mapping image of the heterojunction device. Scale bar: 5 μm . Bottom panel: Thickness of the MoS₂ and TaS₂ flakes along the green dashed arrow in the top panel.

Raman spectroscopy is a useful tool to characterize CDW phase transitions in 1T-TaS₂^{41,42,43,44,45}. When the crystal has not undergone any CDW phase transition, due to the high symmetry of the crystal, specific zone center phonons participate in the first order Raman scattering in order to maintain both energy and momentum conservation. However, once a CDW phase change sets in, the lattice distorts, reducing the translational symmetry of the crystal. This relaxes the condition of first order Raman scattering at the zone center and results in a large number of Raman active vibrational modes⁴¹. Fig. 2a shows the acquired Raman spectra from 1T-TaS₂ in the heating cycle using a 532 nm laser excitation at 193 K (C phase) and 300 K (NC phase), which are in agreement with previous reports^{41,42,45}. In the C phase, the distinct Raman peaks at the lower frequencies (between 90 cm^{-1} and 140 cm^{-1}) result from acoustic branches and directly correlate with the signature of the commensurate nature of the C phase. The higher frequency peaks (between 200 cm^{-1} to 400 cm^{-1}) originate from optical phonons⁴², and can be observed in both C and NC phases. Fig. 2b depicts the resistance (R) - temperature (T) characteristics of a representative two-probe TaS₂ device (in the inset) in vacuum in the heating cycle under small electric field condition. Each layer of 1T-TaS₂ crystal structure is composed of tantalum (Ta) atoms, which are surrounded by sulphur atoms in an octahedral arrangement¹³. The high resistance state at low temperature results from the C phase, where the *David-star* structure^{6,46}, as depicted in Fig. 2c, forms a commensurate structure with the underlying lattice. This commensurate phase results from the inward

displacement of the twelve Ta atoms, located at the star corners, towards the thirteenth Ta atom at the center of the star. The atomic displacement results in the deformation in the structure, including a swelling at the star center^{30,47}. The reduction in the interatomic distance strengthens the bonds inside the David-star in comparison to the bonds outside the star, resulting in the disintegration of the band structure into submanifolds. The twelve corner Ta atoms of the star contribute electrons to the two three-band submanifolds in the valence band, whereas the thirteenth atom at the center of the star contributes one electron to the submanifold in the conduction band (Fig. 2d – left panel). It has been suggested that the spin-orbit coupling forces further reconstruction in the band structure and results in a unique narrow band at the Fermi level that is partially filled^{48,49}. This facilitates electron-electron interaction induced Mott transition in the lattice and a Mott gap opens up (Fig. 2d – right panel)^{47,49}.

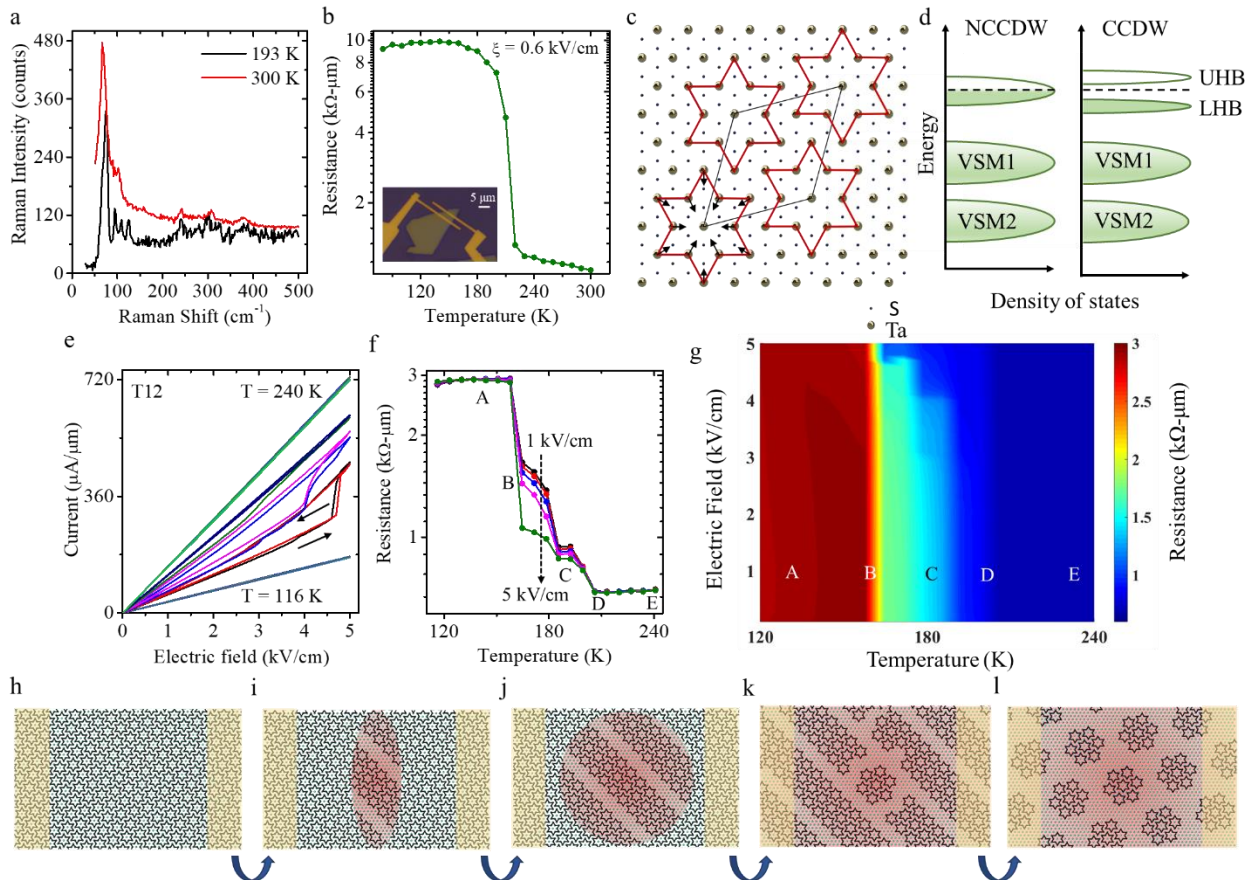


Figure 2. Electrical tuning of phase transitions in 1T-TaS₂. (a) Raman shift of 1T-TaS₂ in NC phase (at 300 K in red) and in C phase (at 193 K in black) during the heating cycle. (b) Temperature dependent resistance of a representative TaS₂ flake under low field condition. Inset: Optical image of the device. (c) David star structure formation in the C phase of 1T-TaS₂. (d) Hubbard model of 1T-TaS₂ depicting Mott gap opening. (e) Current – electric field characteristics of 1T-TaS₂ two probe device (TS12 – probing terminals 1 and 2 in Fig. 1a-b) in the temperature range 116 K to 240 K. The black arrows indicate the bias sweep direction. (f) Resistance – temperature plot of the forward sweep in (e) indicating multiple resistance states. (g) Colour plot of resistance in the temperature-field space. (h)-(l) Joule heating induced localized phases of the device giving rise to multiple resistance states in (f).

Electrically accessing different TaS₂ phases: In order to access the different CDW phases of TaS₂ electrically, we next apply a high field across the probes 1 and 2 of the TaS₂ device TS12 in Fig. 1a. The hysteretic bi-stable switching, as observed in Fig. 2e, is indicative of external bias controlled phase change of the TaS₂ flake. The sharp change in resistance is observed around 160 K (Fig. 2f), which is lower than the C-T phase transition temperature (~ 220 K) under low field in Fig. 2b. This suggests that Joule heating induced increase in local temperature plays a key role in the phase change. A color phase plot of the different resistance-states in the temperature-electric field space is shown in Fig. 2g.

We construct a simple model for the multi-state resistance switching in the TaS₂ flake, as explained in Fig. 2h-l. Initially, at low temperature, the whole flake is in C phase, with linear current-field characteristics (Fig. 2h). This situation is denoted by point A in Fig. 2f-g. As the sample is heated close to the C-T phase transition temperature (T_{CT}), the current induced Joule heating drives the local temperature at the central part of the flake (which is farthest from contact heat sinks) at a higher value than the rest of the flake. Note that, in the C phase, particularly, close to T_{CT} , an

increase in the temperature results in a steep reduction in the lattice component of the thermal conductivity, suppressing the overall thermal conductivity⁵⁰. This provides a positive feedback and further helps to increase the local temperature. Eventually, the temperature of the central part is driven beyond T_{CT} , forcing a local C-T phase transition (point B), as schematically depicted in Fig. 2i. This corresponds to a steep jump in the overall resistance of the sample. With further increase in the drain field or heating of the sample (point C), the local temperature of the surrounding portion also increases causing a gradual increase in the size of the central T phase region (Fig. 2j), and, in turn, results in the gradual reduction in the resistance. When the temperature and field are increased further, the whole flake is eventually converted into T phase (Fig. 2k), and no further change in resistance is observed beyond this point (point D). At higher temperature (point E - beyond 283 K lattice temperature), the whole flake transforms into NC phase (Fig. 2l), however, T-NC phase transition has an almost negligible impact on further change in resistance^{11,13}. The above-mentioned Joule heating induced phase transition mechanism is qualitatively supported by the hysteresis observed in the current-field plot in Fig. 2e. The flake undergoes a C-T phase transition due to Joule heating in the forward sweep. When the field is withdrawn, Joule heating is suppressed, but the flake does not immediately come back to high resistance C phase until the flake cools down below 180 K, resulting in hysteresis.

Efficient carrier injection by 1T-TaS₂ contact: We next explore the carrier injection efficiency from 1T-TaS₂ to 2H-MoS₂ in the heterojunction device (H23) shown in Fig. 1a, by probing the terminals 2 and 3. We take TaS₂ and Ni as the source (S) and the drain (D), respectively, in the rest of the paper. Thus, owing to the asymmetric design of the device, for $V_d (= V_{32}) > 0$, electrons are injected from the TaS₂ contact, while for $V_d < 0$, electrons are injected from Ni into the MoS₂ channel. Hence, by switching the polarity of V_d , we can probe the carrier injection from individual

contacts, as schematically depicted in the insets of Fig. 3a-b. The transfer characteristics of the device for the two cases, shown in Fig. 3a-b at $T = 240$ K (T-phase), indicate an on-off ratio in excess of 10^6 , irrespective of the carriers being injected from Ni or TaS₂. Fig. 3c shows the output characteristics at different back gate voltages (V_g). We clearly observe that the magnitude of the drive current is similar for both TaS₂ and Ni injection cases, suggesting excellent carrier injection efficiency of TaS₂/MoS₂ interface. Such highly efficient carrier injection from the TaS₂/MoS₂ junction is promising for vdW-vdW contact engineering.

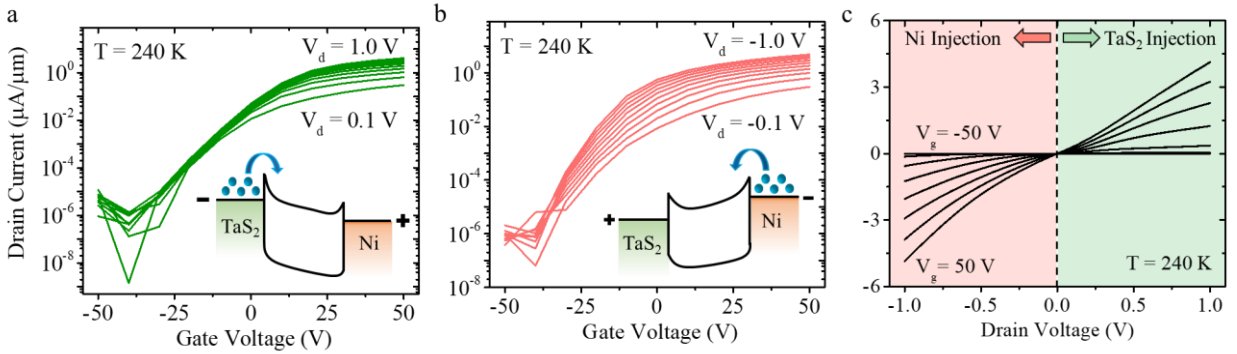


Figure 3. Current-voltage characteristics of the heterojunction device H23. Probing terminal 2 and 3 in Fig. 1a-b. (a)-(b) Transfer characteristics at 240 K (T phase) at different drain voltages, with (a) $V_d > 0$ (Ni is under positive bias and TaS₂ sourcing electrons) and (b) $V_d < 0$ (TaS₂ is under positive bias and Ni sourcing electrons). (c) Output characteristics of the same device.

Modulating drive current by C-T phase transition: We next turn our attention to the control of the carrier injection as the phase of the 1T-TaS₂ source undergoes a C-T phase transition. The two different situations are schematically depicted in Fig. 4a-b. Note that, in this heterojunction device, the overall current density through the TaS₂ source is smaller compared to the high field case discussed in Fig. 2e (TS12) owing to the series resistance offered by the MoS₂ channel, and hence

the role of local Joule heating in the phase transition in TaS₂ source can be ruled out. This results in a more uniform phase transition in TaS₂ source controlled by the external temperature. The measured device current with $V_d > 0$ and $V_d < 0$ are plotted as a function of temperature in Fig. 4c and 4d, respectively. The effect of the TaS₂ phase change on the device current manifests as a sharp increase in the drive current for both TaS₂ and Ni injection, as indicated by the black arrows. The change in drain current (I_d) can be attributed to the change in the series resistance offered by the TaS₂ portion of the device due to the C-T phase transition. The fractional enhancement of drive current during phase change is stronger at higher V_g due to reduced MoS₂ channel resistance.

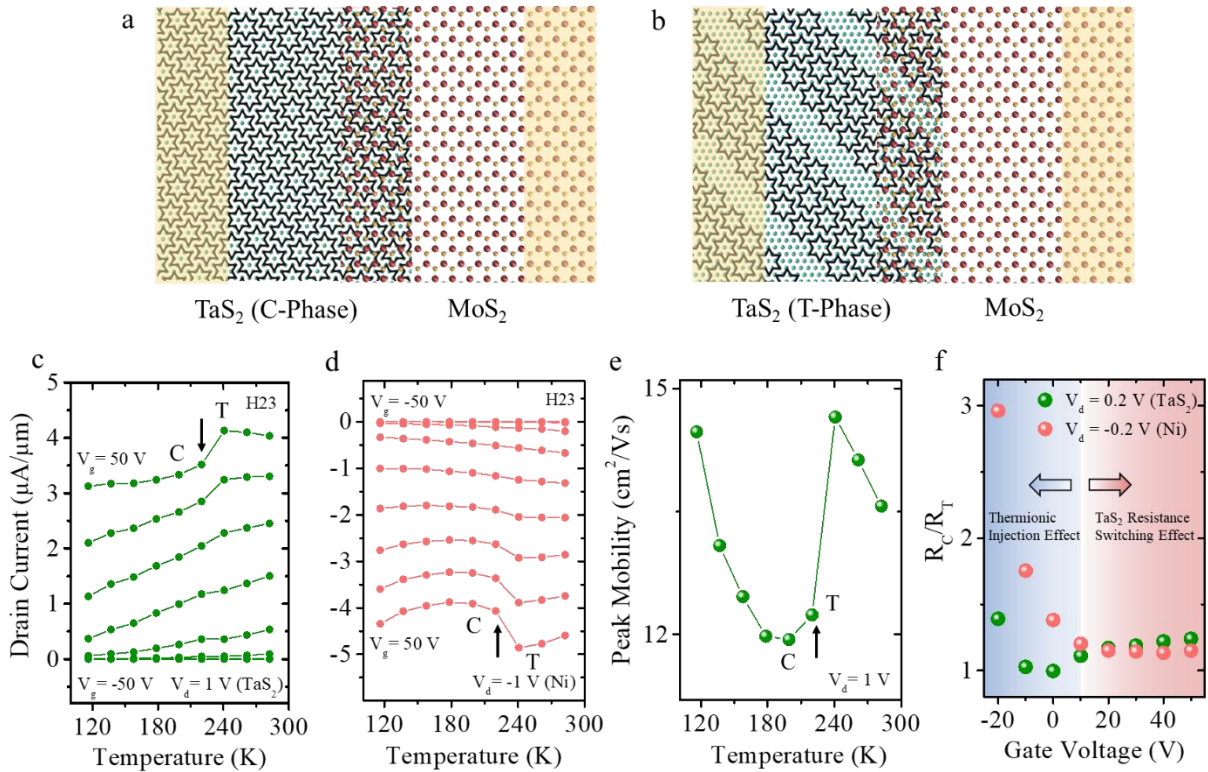


Figure 4. Drive current impact of C-T phase transition in 1T-TaS₂/2H-MoS₂ heterojunction device. (a)-(b) Schematic of the heterojunction with TaS₂ in C-phase [in (a)] and in T-phase [in (b)]. (c)-(d) Drive current of device H23 under $V_d > 0$ [in (c)] and $V_d < 0$ [in (d)]. The C-T phase transition temperature of TaS₂ is indicated by black arrows. (e) Temperature dependent peak

extrinsic mobility of H23. (f) Resistance ratio ($\rho = R_C/R_T$) dependence on the gate voltage for TaS₂ injection ($V_d = 0.2$ V) and Ni injection ($V_d = -0.2$ V).

The MoS₂ extrinsic electron mobility (i.e., the effect of series resistance in mobility calculation has not been de-embedded) in the heterojunction device has been extracted by using the relation:

$$\mu = \frac{L}{WC_{ox}V_d} \times \frac{dI_d}{dV_g}$$

where L is the channel length, W is the channel width, C_{ox} is the back-gate oxide capacitance. The peak extrinsic mobility decreases with an increase in temperature, as shown in

Fig. 4e. Note that the suppression in the TaS₂ series resistance manifests itself by the sharp increase in the peak extrinsic mobility at the phase transition temperature, indicated by the black arrow.

Fig. 4f shows the gate voltage dependence of the ratio of the measured resistances in the C-phase and the T-phase ($\rho = R_C/R_T$). Here, we define R_C and R_T as the total resistance measured right before (at 220 K) and right after (at 240 K) C-T phase transition. At large negative V_g , the total resistance is governed by thermionic injection over the source-channel barrier and consequently the ratio exponentially increases for the Ni injection case ($V_d = -0.2$ V) due to an increase in the temperature. However, at large positive V_g , where the current injection is dominated by tunneling through the Schottky barrier, the ratio becomes close to unity, but remains larger than 1. In fact, at larger positive V_g , the ratio increases with an increase in V_g . This effect is slightly more prominent in the TaS₂ injection ($V_d = 0.2$) case. Such an increase in the ratio is due to a gradual reduction in the MoS₂ channel resistance with V_g , and hence the effect due to TaS₂ series resistance change becomes more pronounced.

Phase transition induced SBH modulation and extraction of TaS₂ C-phase Mott gap: In Fig. 4f, we observe a surprisingly large difference in the ratio ρ in the TaS₂ and Ni injection cases when V_g is below threshold voltage. ρ is found to be suppressed and strongly non-monotonic in V_g at

large negative V_g for the TaS₂ injection case, where the carrier injection is governed by thermionic injection over the Schottky barrier height. This suggests a change in the barrier height at the TaS₂/MoS₂ interface due to the C-T phase change. To explore the SBH at the TaS₂/MoS₂ heterojunction, in Fig. 5a, we plot the H23 drain current (in log scale) at $V_d = 0.1$ V as a function of temperature, for different gate voltages. As indicated by the dashed box, the device current is found to be suppressed by the C-T phase transition at low gate voltages, although this effect smears out at higher gate voltage. This suppression of current is in contrary to the current enhancement effect at large V_g in Fig. 4c. Note that at such a low gate voltage, the channel resistance is high, hence TaS₂ series resistance or channel mobility do not play any role in such flattening of the device current. This indicates an increase in the SBH at the TaS₂/MoS₂ contact interface once the phase change in TaS₂ sets in. At small V_g , the current injection is completely governed by thermionic emission over the TaS₂/MoS₂ barrier. An increase in the temperature increases the thermionic emission probability, but the C-T phase change abruptly increases the SBH, compensating for the temperature increase effect. Note that, no such current suppression behavior is observed when Ni injects the electrons (i.e., for $V_d < 0$) into MoS₂ channel (dashed rectangular box in Fig. 5b). This is due to lack of any phase change of the Ni source, unlike TaS₂, hence SBH at the Ni source remains the same before and after T_{CT} .

We extract the total effective barrier (φ_B) offered by the TaS₂/MoS₂ junction at a given V_g using Richardson equation. As recently proposed³⁹, we use a modified Richardson equation for such a top contact geometry: $I_d = A^*T^\alpha e^{-q\varphi_B/k_B T}$ where $1 \leq \alpha \leq 1.5$. This differs in the power of T from the Richardson equation typically used for the interface between a metal and a conventional bulk semiconductor owing to a change in the dimensionality. φ_B is extracted from the slope of

$\log(\frac{I_d}{T^\alpha})$ versus $\frac{q}{k_B T}$ as depicted in Fig. 5c. One could clearly observe the abrupt increase in the slope as the phase transition happens, indicating an increase in φ_B in the T phase. The extracted φ_B is plotted in Fig. 5d as a function of V_g for both C and T phases. We note here that, the extracted φ_B is not very reliable at large positive V_g due to strong tunneling current and mobility degradation with temperature, which tend to underestimate the extracted effective barrier height.

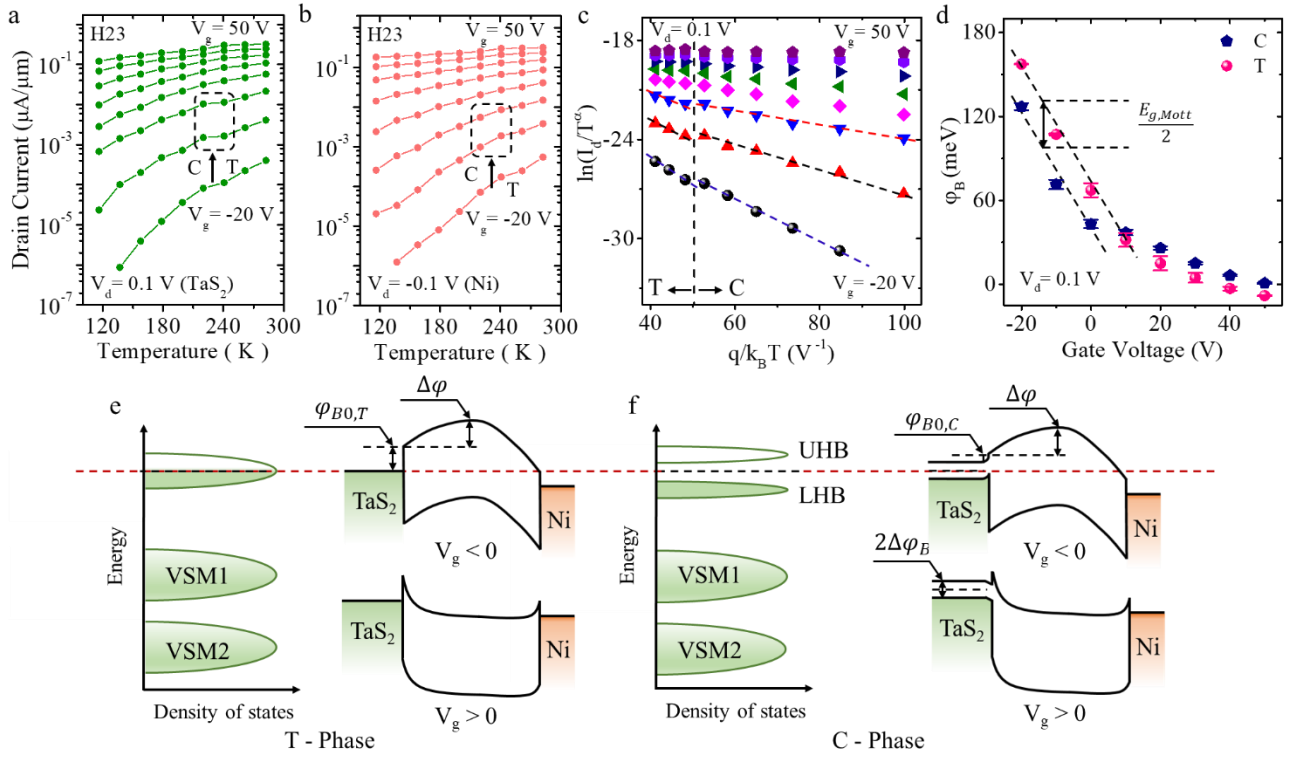


Figure 5. Phase dependent Schottky barrier height at 1T-TaS₂/2H-MoS₂ interface of H23 and Mott gap estimation in C-Phase of 1T-TaS₂. (a) Drain current as a function of temperature under small positive drain bias (TaS₂ injection). The dashed box indicates the suppression of drain current by the C-T phase transition under low V_g , which smears out at higher V_g . (b) Drain current as a function of temperature under small negative drain bias (Ni injection), showing no such suppression in the dashed box. (c) Richardson plot (with $\alpha = 1$) at different gate voltages in two different phases, indicating a C-T phase transition driven change in slope at negative V_g due to

change in barrier height. (d) Extracted barrier height plotted as a function of gate voltage in two different phases. The dashed parallel lines indicate linear increase of barrier height for larger negative V_g . (e)-(f) Schematic representation of the barrier height increase mechanism from C-phase to T-phase.

In Fig. 5d, extracted barrier height is found to increase linearly with decrease in V_g when V_g is small. The ‘*knee point*’ in the curve, where the barrier height deviates from linearity, is indicative of the true Schottky barrier height φ_{B0} (i.e. under flat band condition) of the TaS₂/MoS₂ interface⁵¹. This is much lower compared with the difference between the work function of 1T-TaS₂ (5.2 eV)⁵² and the electron affinity of multi-layer MoS₂ (4 eV)^{53,54}. This suggests a strong Fermi level pinning at the interface, close to the conduction band edge of MoS₂ – supporting the excellent carrier injection efficiency through the interface. Such a strong Fermi level pinning is a unique feature of TaS₂/MoS₂ vdW contact, suggesting the vdW gap does not efficiently suppress the evanescent wave function of the TaS₂ states, likely resulting in metal induced gap states (MIGS)⁵⁵ in MoS₂.

Note that the increase in barrier height with negative V_g in C and T phases can be fitted by two parallel lines, as shown in Fig. 5d. This observation indicates that the band bending ($\Delta\varphi$) in MoS₂ is similar in both cases at large negative V_g . This is schematically explained in Fig. 5e-f, which allows us to write the total barrier as: $\varphi_{B,p}(V_g) = \varphi_{B0,p} + \Delta\varphi(V_g)$, where $\varphi_{B0,p}$ is the true SBH of the TaS₂/MoS₂ interface (under flat-band condition) and $p \in \{C, T\}$ represents the phase of TaS₂. Assuming a symmetric Mott gap opening, $\Delta\varphi_B$ provides an estimate of the Mott gap in TaS₂ in the C phase:

$$\Delta\varphi_B = \varphi_{B,T} - \varphi_{B,C} \approx \varphi_{B0,T} - \varphi_{B0,C} \approx \frac{E_{g,Mott}}{2}$$

The vertical separation of the dashed fitting lines in Fig. 5d is an indicator of $\Delta\phi_B$. The extracted Mott gap of TaS₂ in the C-phase is estimated to be $E_{g,Mott} \approx 71 \pm 7$ meV. This is in reasonable agreement with reported numbers in literature from different optical techniques viz. infrared reflectivity^{20,21}, time resolved photoemission spectroscopy^{9,22}, angle resolved photoemission spectroscopy^{10,23,24} and angle resolved inverse photoemission spectroscopy²⁵ – providing an independent verification using pure electrical transport method.

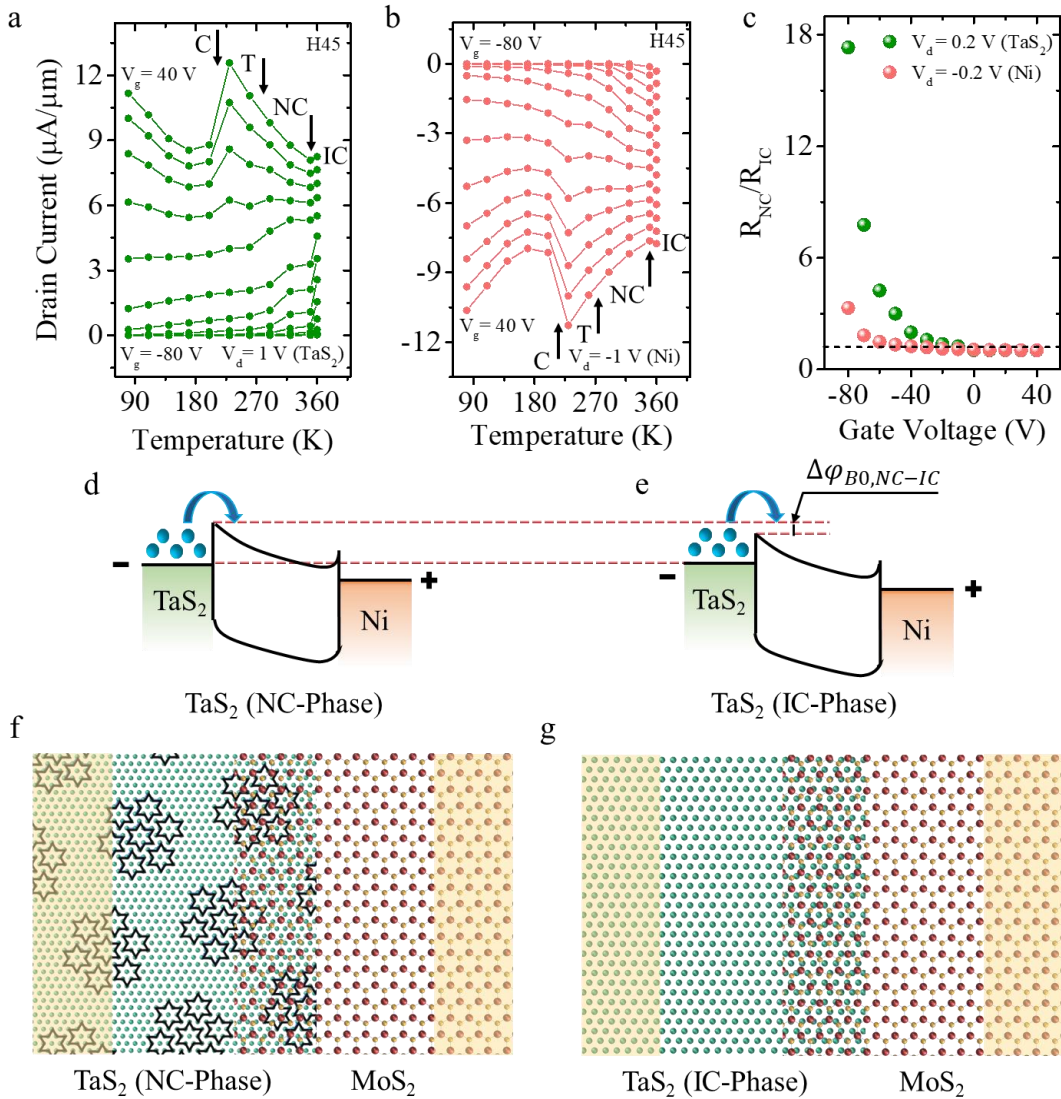


Figure 6. Enhanced resistance switching during NC-IC phase transition in 1T-TaS₂/2H-MoS₂ heterojunction device H45. (a)-(b) Drive current of device H45 under $V_d > 0$ [in (a)] and $V_d < 0$ [in (b)]. The different phase transition temperatures of TaS₂ are indicated by black arrows. (c) Resistance ratio (R_{NC}/R_{IC}) as the function of gate voltage for TaS₂ injection (in green symbols, $V_d = 0.2 V$) and Ni injection (in orange symbols, $V_d = -0.2 V$). The dashed line indicates 1T-TaS₂ control. (d)-(e) Schematic for SBH height reduction from NC [in (d)] to IC-phase [in (e)]. (f)-(g) Schematic of the heterojunction with TaS₂ in NC-phase [in (f)] and in IC-phase [in (g)].

Enhancing resistance switching during NC-IC phase transition: Fig. 6a-b depict the temperature dependent drain current characteristics from another device (H45) possessing a lower threshold voltage than H23, and the device is driven deep into the inversion by increasing the overdrive voltage. An optical image of the device H45, along with the control TaS₂ transport characteristics are provided in **Supplemental Material S2**⁴⁰. In this device, we could modulate the drive current by as much as ~40% through the C-T phase change under large gate overdrive condition. The strong suppression of the drive current at higher temperatures (beyond 223 K) is due to the temperature induced mobility degradation effect. The temperature dependent peak extrinsic mobility extracted from H45 is shown in **Supplemental Material S2**⁴⁰. When we drive the temperature of the device up to 360 K, which is beyond the NC-IC phase transition temperature at 353 K, we observe that the NC-IC phase transition manifests as a step jump in the drive current, both for TaS₂ and Ni injection cases as in Fig. 6a and b, respectively. The corresponding resistance switching ratios ($\frac{R_{NC}(T=350 K)}{R_{IC}(T=360 K)}$) at $V_d = \pm 0.2 V$ are plotted in Fig. 6c. For reference, we also show the ratio for the TaS₂ control as a dashed line in the same plot. For TaS₂ injection case ($V_d = 0.2$), the switching ratio is a strong function of V_g and is remarkably large at negative V_g reaching a value of 17.3 at $V_g = -80 V$, which is 14.5 times higher than the TaS₂ control device. On the other hand,

the ratio remains a weak function of V_g for Ni injection case and remains close to the value of TaS₂ control.

These observations point to a suppression of the SBH at the TaS₂/MoS₂ interface due to the NC-IC phase transition, as schematically depicted in Fig. 6d-g. Consequently, for electron injection from TaS₂ source, the current modulation is much higher, while for Ni injection, we only get small effect due to a change in the series resistance of TaS₂ during the phase transition. While the origin of such a change in SBH requires further investigation, it is likely that during the NC-IC phase transition, as the hexagonal David-star clusters are broken (Fig. 6f-g) to increase conductivity, there is a more pronounced effect of the MIGS from TaS₂ into the bandgap of MoS₂. This causes the Fermi level to be pinned closer to the conduction band edge of MoS₂, reducing the SBH.

Conclusion:

In conclusion, we have demonstrated a low-barrier efficient electrical contact between 1T-TaS₂ source and 2H-MoS₂ channel, which is promising for “all-2D” flexible electronics. Along with the usual conductivity switching of 1T-TaS₂ during different phase transitions, we discovered that these transitions also bring about a change in the Schottky barrier height at the 1T-TaS₂/2H-MoS₂ interface. The phase transition driven resistance switching ratio of the heterojunction thus shows a large modulation that can be controlled by an external gate voltage. This enhancement and additional gate control provide an unprecedented opportunity for boosting different device applications which exploit such phase transition induced resistance switching, such as broadband photodetection, neuromorphic circuits, negative differential conductance and fast oscillator.

Acknowledgements:

K. M. acknowledges the support a grant from Indian Space Research Organization (ISRO), grants under Ramanujan Fellowship, Early Career Award, and Nano Mission from the Department of Science and Technology (DST), Government of India, and support from MHRD, MeitY and DST Nano Mission through NNetRA.

Conflicts of Interest:

The authors declare no conflict of interest.

References:

1. Butler, S. Z. *et al.* Progress, challenges, and opportunities in two-dimensional materials beyond graphene. *ACS Nano* **7**, 2898–2926 (2013).
2. Jariwala, D., Sangwan, V. K., Lauhon, L. J., Marks, T. J. & Hersam, M. C. Emerging device applications for semiconducting two-dimensional transition metal dichalcogenides. *ACS Nano* **8**, 1102–1120 (2014).
3. Akinwande, D., Petrone, N. & Hone, J. Two-dimensional flexible nanoelectronics. *Nat. Commun.* **5**, 1–12 (2014).
4. Thorne, R. E. Charge-density-wave conductors. *Phys. Today* **49**, 42–47 (1996).
5. Grüner, G. The dynamics of charge-density waves. *Rev. Mod. Phys.* **60**, 1129–1181 (1988).
6. Wilson, J. A., Di Salvo, F. J. & Mahajan, S. Charge-density waves and superlattices in the metallic layered transition metal dichalcogenides. *Adv. Phys.* **24**, 117–201 (1975).
7. Williams, P. M., Scruby, C., Clark, W. & Parry, G. Charge Density Waves in the Layered Transition Metal Dichalcogenides. *J. Phys. Colloq.* **37 (C4)**, C4 139-C4 150 (1976).

8. Sipos, B. *et al.* From Mott state to superconductivity in 1T-TaS₂. *Nat. Mater.* **7**, 960–965 (2008).
9. Hellmann, S. *et al.* Ultrafast melting of a charge-density wave in the mott insulator 1T-TaS₂. *Phys. Rev. Lett.* **105**, 187401 (2010).
10. Rossnagel, K. On the origin of charge-density waves in select layered transition-metal dichalcogenides. *J. Phys. Condens. Matter* **23**, 213001 (2011).
11. Manzke, R. *et al.* On the phase transitions in 1T-TaS₂. *Europhys. Lett.* **8**, 195–200 (1989).
12. Ishiguro, T. & Sato, H. Electron microscopy of phase transformations in 1T-TaS₂. *Phys. Rev. B* **44**, 2046–2060 (1991).
13. Thomson, R. E., Burk, B., Zettl, A. & Clarke, J. Scanning tunneling microscopy of the charge-density-wave structure in 1T-TaS₂. *Phys. Rev. B* **49**, 16899–16916 (1994).
14. Tani, T., Osada, T. & Tanaka, S. The pressure effect on the CDW-transition temperatures in 1T-TaS₂. *Solid State Commun.* **22**, 269–272 (1977).
15. Di Salvo, F. J., Wilson, J. A., Bagley, B. G. & Waszczak, J. V. Effects of doping on charge-density waves in layer compounds. *Phys. Rev. B* **12**, 2220–2235 (1975).
16. Ang, R. *et al.* Real-space coexistence of the melted Mott state and superconductivity in Fe-substituted 1T-TaS₂. *Phys. Rev. Lett.* **109**, 176403 (2012).
17. Yoshida, M. *et al.* Controlling charge-density-wave states in nano-thick crystals of 1T-TaS₂. *Sci. Rep.* **4**, 07302 (2014).
18. Yu, Y. *et al.* Gate-tunable phase transitions in thin flakes of 1T-TaS₂. *Nat. Nanotechnol.* **10**, 270–276 (2015).

19. Stojchevska, L.; Vaskivvskyi, I.; Mertelj, T.; Svetin, D.; Brazovskii, S.; Mihailovic, D. Ultrafast Switching to a Stable Hidden Quantum State in an Electronic Crystal. *Science* (80-). **344**, 177–180 (2014).
20. Barker, A. S., Ditzenberger, J. A. & DiSalvo, F. J. Infrared study of the electronic instabilities in tantalum disulfide and tantalum diselenide. *Phys. Rev. B* **12**, 2049–2054 (1975).
21. Gasparov, L. V. *et al.* Phonon anomaly at the charge ordering transition in 1T-TaS₂. *Phys. Rev. B - Condens. Matter Mater. Phys.* **66**, 943011–943015 (2002).
22. Perfetti, L. *et al.* Femtosecond dynamics of electronic states in the Mott insulator 1T-TaS₂ by time resolved photoelectron spectroscopy. *New J. Phys.* **10**, 053019 (2008).
23. Pollak, R. A., Eastman, D. E., Himpsel, F. J., Heimann, P. & Reihl, B. 1T-TaS₂ charge-density-wave metal-insulator transition and Fermi-surface modification observed by photoemission. *Phys. Rev. B* **24**, 7435–7438 (1981).
24. Pillo, T. *et al.* Fine structure in high-resolution photoemission spectra of quasi-two-dimensional 1T-TaS₂. *Phys. Rev. B* **64**, 245105 (2001).
25. Sato, H. *et al.* Conduction-band electronic structure of 1 T -TaS₂ revealed by angle-resolved inverse-photoemission spectroscopy. *Phys. Rev. B - Condens. Matter Mater. Phys.* **89**, 155137 (2014).
26. Wu, Dong; Ma, Y. C.; Niu, Y. Y.; Liu, Q. M.; Dong, Tao; Zhang, S. J.; Niu, J. S.; Zhou, H. B.; Wei, Jian; Wang, Y. X.; Zhao, Z. R.; Wang, N. L. Ultrabroadband photosensitivity from visible to terahertz at room temperature. *arXiv:1806.08952*

27. Liu, G. *et al.* A charge-density-wave oscillator based on an integrated tantalum disulfide-boron nitride-graphene device operating at room temperature. *Nat. Nanotechnol.* **11**, 845–850 (2016).
28. Khitun, A., Liu, G. & Balandin, A. A. Two-dimensional oscillatory neural network based on room temperature charge-density-wave devices. *IEEE Trans. Nanotechnol.* **16**, 1–8 (2017).
29. Young, P. a. Lattice parameter measurements on molybdenum disulphide. *J. Phys. D. Appl. Phys.* **1**, 936–938 (1968).
30. Spijkerman, A., de Boer, J. L., Meetsma, A., Wiegers, G. A. & van Smaalen, S. X-ray crystal-structure refinement of the nearly commensurate phase of 1T-TaS₂ in (3+2)-dimensional superspace. *Phys. Rev. B* **56**, 13757 (1997).
31. Lee, Y. T. *et al.* Graphene versus ohmic metal as source-drain electrode for MoS₂ nanosheet transistor channel. *Small* **10**, 2356–2361 (2014).
32. Du, Y. *et al.* MoS₂ Field-Effect transistors with graphene/metal heterocontacts. *IEEE Electron Device Lett.* **35**, 599–601 (2014).
33. Leong, W. S. *et al.* Low resistance metal contacts to MoS₂ devices with nickel-etched-graphene electrodes. *ACS Nano* **9**, 869–877 (2015).
34. Andleeb, S., Eom, J., Naz, N. R. & Singh, A. K. MoS₂ field effect transistor with graphene contacts. *J. Mater. Chem. C* **5**, 8308–8314 (2017).
35. Sata, Y. *et al.* N- and p-type carrier injections into WSe₂ with van der Waals contacts of two-dimensional materials. *Jpn. J. Appl. Phys.* **56**, 04CK09 (2017).

36. Shin, H. G. *et al.* Vertical and In-Plane Current Devices Using NbS₂/n-MoS₂ van der Waals Schottky Junction and Graphene Contact. *Nano Lett.* (2018). doi:10.1021/acs.nanolett.7b05338
37. Yang, L. *et al.* Chloride molecular doping technique on 2D materials: WS₂ and MoS₂. *Nano Lett.* **14**, 6275–6280 (2014).
38. English, C. D., Shine, G., Dorgan, V. E., Saraswat, K. C. & Pop, E. Improved contacts to MoS₂ transistors by ultra-high vacuum metal deposition. *Nano Lett.* **16**, 3824–3830 (2016).
39. Somvanshi, D. *et al.* Nature of carrier injection in metal/2D-semiconductor interface and its implications for the limits of contact resistance. *Phys. Rev. B* **96**, 205423 (2017).
40. See Supplemental Material at [xxx] for output characteristics of MoS₂ channel with Ni contact on both sides, characteristics of TaS₂ control and heterojunction from device H45.
41. Smith, J. E., Tsang, J. C. & Shafer, M. W. Raman spectra of several layer compounds with charge density waves. *Solid State Commun.* **19**, 283–286 (1976).
42. Duffey, J. R., Kirby, R. D. & Coleman, R. V. Raman scattering from 1T-TaS₂. *Solid State Commun.* **20**, 617–621 (1976).
43. Sugai, S.; Murase, K.; Uchida, S.; Tanaka, S. Comparison of the soft modes in Tantalum Dichalcogenides. *Phys. B+C* **105**, 405–409 (1981).
44. Fu, W. *et al.* Controlled Synthesis of Atomically Thin 1T-TaS₂ for Tunable Charge Density Wave Phase Transitions. *Chem. Mater.* **28**, 7613–7618 (2016).
45. He, R. *et al.* Distinct surface and bulk charge density waves in ultrathin 1T-TaS₂. *Phys. Rev. B* **94**, 201108 (2016).

46. Tosatti, E. & Fazekas, P. On the nature of the low-temperature phase of 1T-TaS₂. *J. Phys. Colloq.* **37**, C4-165-C4-168 (1976).
47. Fazekas, P. & Tosatti, E. Electrical , structural and magnetic properties of pure and doped 1T-TaS₂. *Philos. Mag. B* **39**, 229–244 (1979).
48. Smith, N. V, Kevan, S. D. & DiSalvo, F. J. Band structures of the layer compounds 1T-TaS₂ and 2H-TaSe₂ in the presence of commensurate charge-density waves. *J. Phys. C Solid State Phys.* **18**, 3175–3189 (1985).
49. Rossnagel, K. & Smith, N. V. Spin-orbit coupling in the band structure of reconstructed 1T-TaS₂. *Phys. Rev. B* **73**, 073106 (2006).
50. Núñez-Regueiro, M., Lopez-Castillo, J. & Ayache, C. Thermal Conductivity of 1T-TaS₂ and 2H-TaSe₂. *Phys. Rev. Lett.* **55**, 1931–1934 (1985).
51. Das, S., Chen, H. Y., Penumatcha, A. V. & Appenzeller, J. High performance multilayer MoS₂ transistors with scandium contacts. *Nano Lett.* **13**, 100–105 (2013).
52. Shimada, T. & Ohuchi, F. S. Work Function and Photothreshold of Layered Metal Dichalcogenides. *Jpn. J. Appl. Phys.* **33**, 2696–2698 (1994).
53. Schlaf, R., Lang, O., Pettenkofer, C. & Jaegermann, W. Band lineup of layered semiconductor heterointerfaces prepared by van der Waals epitaxy: Charge transfer correction term for the electron affinity rule. *J. Appl. Phys.* **85**, 2732–2753 (1999).
54. Howell, S. L. *et al.* Investigation of Band-Offsets at Monolayer-Multilayer MoS₂ Junctions by Scanning Photocurrent Microscopy. *Nano Lett.* **15**, 2278–2284 (2015).
55. Tersoff, J. Schottky Barrier Heights and the Continuum of Gap States. *Phys. Rev. Lett.* **52**,

465–468 (1984).

Supplemental Material:

Gate controlled large resistance switching driven by charge density wave in 1T-TaS₂/2H-MoS₂ heterojunction

Mehak Mahajan^{||}, Krishna Murali^{||}, Nikhil Kawatra, and Kausik Majumdar^{*}

Department of Electrical Communication Engineering, Indian Institute of Science, Bangalore
560012, India

^{||}These authors contributed equally

^{*}Corresponding author, *email: kausikm@iisc.ac.in*

Supplemental Material S1:

Output characteristics of MoS₂ channel with Ni contact on both sides

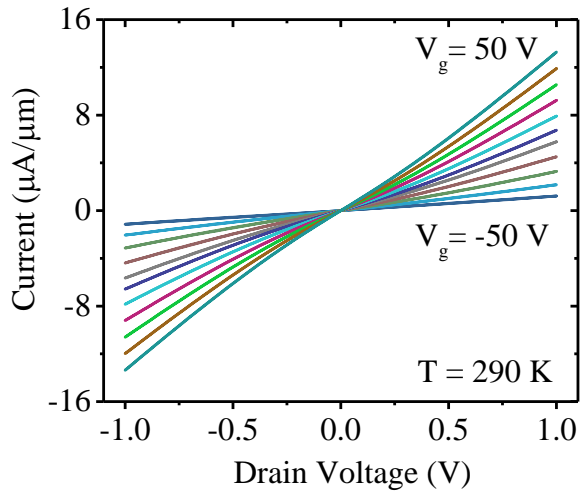


Figure S1. I_d - V_d characteristics of MoS₂ channel with Ni contact on both sides for different gate voltages, at $T = 290$ K, with channel length of $2.8 \mu\text{m}$.

Supplemental Material S2:

Characteristics of TaS₂ control and heterojunction from device H45

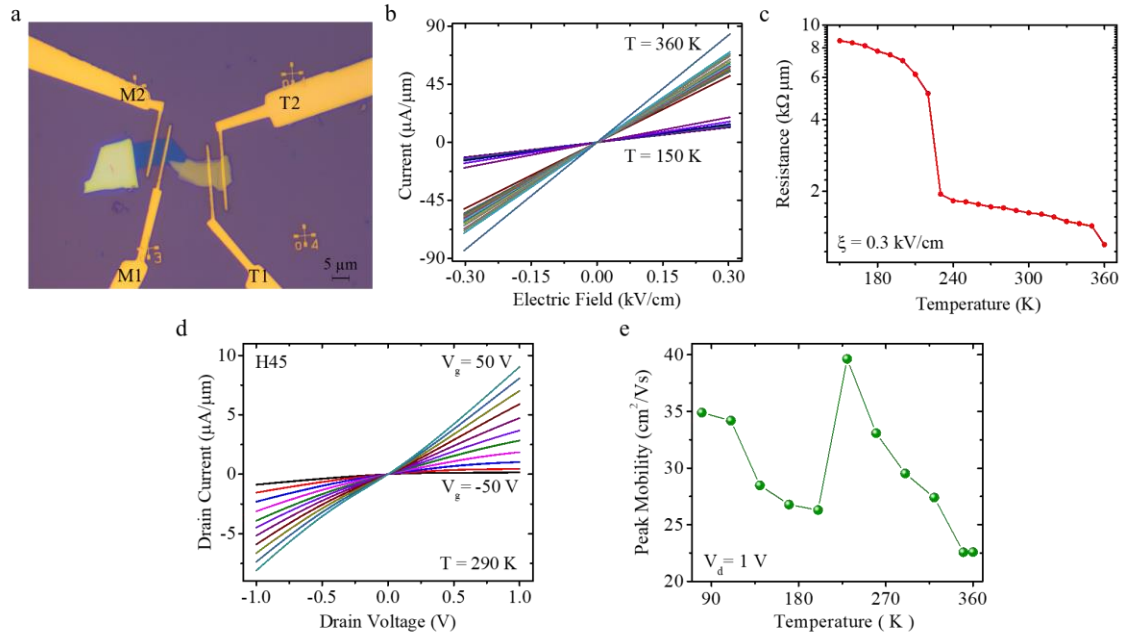


Figure S2. (a) Optical image of the heterojunction device H45. T1 and T2 are the contacts to the TaS₂ flake, while M1 and M2 are contacts to MoS₂. Scale bar is 5 μm. (b) Current versus electric field characteristics of TaS₂ control (probed between T1 and T2) at different temperatures and low electric field condition. (c) The resistance versus temperature plot extracted from (b) clearly indicating the C-T transition around 220 K and the NC-IC phase transition around 350 K. (d) Output characteristics of the heterojunction H45 (probed between T1 and M1) at 290 K. (e) Temperature dependent peak extrinsic mobility, as extracted from H45.